Dendritic nanoarchitecture imparts ZSM-5 zeolite with enhanced adsorption and catalytic performance in energy applications

María del Mar Alonso-Doncel [a], Cristina Ochoa-Hernández [b], Gema Gómez-Pozuelo [c], Adriana Oliveira [a], José González-Aguilar [d], Ángel Peral [e], Raúl Sanz [c], David P. Serrano [a,e,*]

[a] *Thermochemical Processes Unit, IMDEA Energy Institute, Avda. Ramón de la Sagra, 3, E28935, Móstoles, Madrid, Spain*
[b] *Department of Heterogeneous Catalysis, Max-Planck-Institut für Kohlenforschung, Kaiser-Wilhelm-Platz 1, D45470, Mülheim an der Ruhr, Germany*
[c] *Department of Chemical and Environmental Technology, Rey Juan Carlos University, C/ Tulipán s/n, E28933, Móstoles, Madrid, Spain*
[d] *High Temperature Processes Unit, IMDEA Energy Institute, Avda. Ramón de la Sagra, 3, E28935, Móstoles, Madrid, Spain*
[e] *Department of Chemical, Energy and Mechanical Technology, Rey Juan Carlos University, C/ Tulipán s/n, E28933, Móstoles, Madrid, Spain*

ARTICLE INFO

ABSTRACT

The development of zeolites possessing dendritic features represents a great opportunity for the design of novel materials with applications in a large variety of fields and, in particular, in the energy sector to afford its transition towards a low carbon system. In the current work, ZSM-5 zeolite showing a dendritic 3D nanoarchitecture has been synthesized by the functionalization of protozeolitic nanounits with an amphiphilic organosilane, which provokes the branched aggregative growth of zeolite embryos. Dendritic ZSM-5 exhibits outstanding accessibility arising from a highly interconnected network of radially-oriented mesopores (3 – 10 nm) and large cavities (20 – 80 nm), which add to the zeolitic micropores, thus showing a well-defined trimodal pore size distribution. These singular features provide dendritic ZSM-5 with sharply enhanced performance in comparison with nano- and hierarchical reference materials when tested in a number of energy related applications, such as VOCs (toluene) adsorption (improved capacity), plastics (low-density polyethylene) catalytic cracking (boosted activity) and hydrogen production by methane catalytic decomposition (higher activity and deactivation resistance).

1. Introduction

Materials with dendritic nanoarchitectures have recently attracted considerable attention with a number of ground-breaking findings being achieved over the past 10 years [1]. They possess 3D branched superstructures with outstanding accessibility due to the presence of a highly interconnected network of radially oriented pores [2].

The development of dendritic nanomaterials is undergoing fast progress, extending from pure silica to other compositions (titanium, carbon, bio-active glass and hybrid solids) [1–3]. Accordingly, the terms Dendritic Fibrous Nano Particles (DFNP) and Dendritic Mesoporous Silica Nanospheres (DMSNs) have been recently coined [2,3]. The relevance of these materials relies on their high porosity and accessibility, being explored as supports of a number of guest molecules and functionalities [1,4–6]. In the past years, an increasing number of articles have been published concerning the use of dendritic materials in a variety of fields: catalysis, water treatment, solar-energy harvesting, energy storage, self-cleaning antireflective coatings, surface plasmon resonance-based ultrasensitive sensors, CO_2 capture and biomedical applications [1]. Accordingly, they have been recently considered the "rising stars" of mesoporous materials [3].

On the other hand, zeolites represent a very relevant type of crystalline microporous solids with important industrial applications as catalysts, adsorbents, supports, and ion-exchange agents [7–9]. Despite the high number and diversity of uses already available, the research in zeolites is not levelling off but, on the contrary, there is a fast-expanding interest in zeolite science and technology. This is a consequence of their exceptional properties: crystallinity, high surface area, uniform micropores, shape selectivity, strong and tunable acidity, adjustable hydrophobic/hydrophilic properties, high hydrothermal stability and diversity of structures and compositions.

However, most zeolites possess pore sizes below 1 nm, which is an important drawback for the processing and/or supporting of bulky species. This limitation has motivated an intense research

* Corresponding author.
E-mail address: david.serrano@imdea.org (D.P. Serrano).

effort during the past years aimed at the preparation of zeolites with enhanced accessibility [10–13]. Thereby, a variety of strategies have been pursued, such as those based on the synthesis of nano- and hierarchical zeolites [14–17]. Likewise, a number of zeolite structures have been synthesized in bidimensional form [18–21]. The performance of these new types of zeolitic materials usually overcomes those of conventional zeolites [22]. However, new and disruptive concepts of zeolites showing outstanding accessibility are yet required in many applications and fields, as it is the case of the energy sector in its transition to a low carbon system.

Previous studies adapting the synthesis methods of DFNPs to zeolites have been based on the direct combination of microemulsion systems with zeolite-seed crystallization. The materials so obtained (named as fibrous zeolites), although exhibiting interesting properties, show hybrid core–shell structures, in which the dendritic shell consists of amorphous silica [23–25]. Besides, as a rare example, the synthesis of fractal MTW zeolite has been reported based on dendritic growth via twinning-plane induced crystallization [26].

Therefore, the development of dendritic zeolites remains a relevant scientific and technological challenge. In this way, the present work reports the synthesis and properties of ZSM-5 zeolite with a fully crystalline 3D dendritic nanoarchitecture, which provides it with outstanding accessibility and textural features, as well as with remarkable performance in a number of energy related applications as both adsorbent and catalyst. ZSM-5 is one of the most important zeolites due to its relevant industrial applications in oil refining, petrochemistry, biomass conversion and pollutant removal [27–29]. Accordingly, the development of ZSM-5 zeolite with dendritic features is expected to have a remarkable impact on a variety of fields and in particular in the energy sector.

2. Experimental

2.1. Materials synthesis

The experimental procedure and conditions used for the synthesis of dendritic ZSM-5 were taken from previous literature works [30,31] on the preparation of hierarchical ZSM-5 by means of the so-called seed-silanization approach but employing in this case TPOAC as silanization agent. Thus, dendritic ZSM-5 samples were synthesized first mixing fined milled aluminum isopropoxide (AIP, Sigma-Aldrich, 98%) with tetrapropylammonium hydroxide (TPAOH, Sigma-Aldrich, 40 wt% in water) at room temperature and 300 r min^{-1} of stirring in a round bottom flask until complete dissolution of AIP. Then, a proper amount of tetraethyl orthosilicate (TEOS, Sigma-Aldrich, 98%) was added submerging the flask in an ice-bath during a few minutes, being then stirred at room temperature for 40 h until complete hydrolysis of the silicon source. The molar composition of the initial precursor solution was as follows: Al_2O_3: 60 SiO_2: 11 TPAOH: 1500 H_2O. The alcohols produced as hydrolysis by-products were removed at 75 mbar and 50 °C in a rotatory evaporator. The clear precursor solution was precrystallized under reflux and stirring (300 r min^{-1}) at 90 °C for 20 h. When the precrystallization was completed, the bottom flask was once again submerged in an ice bath for stabilizing the protozeolitic units prior to the addition of dimethyloctadecyl [3-(trimethoxysilyl) propyl] ammonium chloride (TPOAC, Gelest, 60 wt% in methanol). TPOAC was incorporated in a proportion of 5 mol% regarding the initial Si content, which provoked the clear solution to turn into a milky-like mixture in a few seconds, indicating the spontaneous formation of an emulsion. The reactive mixture was maintained at 0 °C and 300 r min^{-1} for 6 h. Then, the

flask content was loaded into a 25 mL Teflon-lined autoclave reactor, being crystallized under different temperatures (150 °C or 170 °C) and times (1–10 days). Thereafter, the autoclaves were cooled down by immersion into an ice bath to suddenly interrupt the crystallization. Two well different phases were found when the autoclaves were opened, a whitish supernatant gel and a white solid phase in the bottom of the Teflon container. At short synthesis times, the whitish supernatant gel was an amorphous material that evolves into a non-dendritic ZSM-5 zeolite as the hydrothermal treatment progresses. The white solid phase contained the dendritic zeolite sample and it was mechanically separated, washed with distilled water, centrifuged at 11,000 r min^{-1} for three times, and dried at 100 °C overnight.

The as-synthesized samples were subjected to a two-step calcination treatment. The first step was carried out under nitrogen flow, heating the sample up to 400 °C (1.8 °C min^{-1}), being kept constant for 4 h. The second calcination step was performed under an air flow by heating up to 550 °C (1.8 °C min^{-1}) and then keeping this temperature constant for 5 h. The samples were identified as d-ZSM-5 (Xd – Y °C), where X and Y are the corresponding crystallization time and temperature, respectively.

To investigate the effect of the TPOAC order addition, a sample was synthesized following the procedure above described but incorporating the amphiphilic organosilane at the beginning of the gel preparation and omitting the precrystallization step. The corresponding gel was hydrothermally treated at 170 °C for 7 days.

In order to assess the effect of the gel concentration, two additional samples were synthesized increasing the initial H_2O/SiO_2 molar ratio to 37.5 and 50. In these experiments, the molar composition of the initial precursor solution was as follows: Al_2O_3: 60 SiO_2: 11 TPAOH: x H_2O, being "x" adjusted to 2250 and 3000, respectively. Another sample was synthesized with the aim to check the role of TPA$^+$ cations with a molar composition of the initial synthesis gel of Al_2O_3: 60 SiO_2: 13.75 TPA: 1500 H_2O. The 2.75 mol excess of TPA referred to the conventional synthesis concentration was added as tetrapropylammonium bromide in order to not disturb the synthesis pH. This sample was denoted as ZSM-5 (1.25 TPA). Also, an additional sample was synthesized with 10 mol% of TPOAC, this sample was denoted as ZSM-5 (10 TPOAC). Finally, a zeolitic sample denoted as ZSM-5 (2.5 NaOH), prepared with the following gel molar composition: Al_2O_3: 60 SiO_2: 11 TPAOH: 1500 H_2O: 1.5 NaOH was synthesized in order to evaluate the effect of the presence of Na$^+$ cations. The synthesis procedure for all of these samples was the same as above described, the crystallization is performed at 170 °C for 7 days.

A commercial nanocrystalline ZSM-5 sample (n-ZSM-5), purchased from Clariant, and a hierarchical ZSM-5 sample (h-ZSM-5) were used as references. The latter was synthesized using a procedure similar to the above described for the dendritic samples starting from the same gel composition (Al_2O_3: 60 SiO_2: 11 TPAOH: 1500 H_2O) but replacing TPOAC by N-phenylaminopropyl trimethoxysilane that was added in 5 mol% regarding the initial Si content. Moreover, for the h-ZSM-5 sample the final mixture was maintained under reflux at 90 °C and 300 r min^{-1} for 6 h. In this case, no noticeable physical changes were detected in the flask liquid content after the addition of the silanization agent. The resulting solution was transferred to a 25 mL Teflon-lined autoclave reactor and crystallized at 170 °C for 7 days. The synthesis products consisted of a clear liquid supernatant over a solid white powder in the bottom of the autoclave. The entire content of the Teflon vessel was centrifuged (11000 r min^{-1}) and washed with water three times. The resulting solid was dried overnight (100 °C) and then subjected to calcination using the same procedure as above indicated for the dendritic ZSM-5 samples.

María del Mar Alonso-Doncel, C. Ochoa-Hernández, G. Gómez-Pozuelo et al.

Journal of Energy Chemistry 80 (2023) 77–88

2.2. Materials characterization

A powder Empyrean PANalytical diffractometer with Cu *K*α radiation (λ = 1.5406 Å) was employed for recording the wide-angle X-ray diffraction patterns of the calcined samples.

Thermogravimetric TG/DTG analyses were performed using an SDT 2960 instrument, loading an alumina crucible with ca. 7 mg of the sample that was heated up to 700 °C (5 °C min^{-1}) under 100 mL min^{-1}.

Transmission Electron Microscopy (TEM) and High angle annular dark field scanning TEM (HAADF-STEM) images were collected using a JEOL F200 CF (200 kV) microscope. This instrument was also employed for the acquisition of tilt series of both TEM and dark-field STEM images of dendritic ZSM-5 particles over an angular range of ± 68° with an increment of 2°. Alignment and processing of these images to obtain the movies included in the Supporting Video files were performed with the ImageJ software. Moreover, dark-field STEM micrographs were visualized using Paraview 5.10.0 open-source software [32]. Images initially recorded in TIFF format were read and represented with the "Turbo" rainbow color map using the same upper and lower limits, which have subsequently been scaled between 0 and 1. Limits were chosen once all images were analyzed to achieve the highest contrast and avoid color saturation. Finally, tomographic reconstruction from tilt series of dark-field STEM micrographs in TIFF format was made with the open-source Tomviz software package (version 1.10.0) [33,34]. Tomogram was processed to identify the dendritic ZSM-5 particle and microscope mesh support, represented using the Viridis and Magma color maps, respectively; and visualize internal particle morphology. Particle slices were represented using the "plasma" color map, with upper and lower limits being selected to achieve the best contrast at the particle boundary.

Aluminum and silicon content of the calcined samples were determined by ICP-OES with a Perking Elmer Optima 7300AD equipment. Fourier transform infrared (FTIR) spectra were measured with a resolution of 4 cm^{-1} in JASCO-4600 instrument equipped with a TGS detector. The type and the concentration of the acid sites were investigated by adsorbing a basic probe molecule (pyridine) and monitoring the changes by FTIR (Brønsted acid sites: 1545 cm^{-1}, ε = 1.67 cm μmol^{-1}; Lewis acid sites: 1455 cm^{-1}, ε = 2.22 cm μmol^{-1}) [35]. In a typical experiment, a self-supported wafer (10 mg cm^{-2}) was prepared and activated in-situ under vacuum at 450 °C for 4 h. Subsequently, pyridine was adsorbed at 150 °C and a thermal desorption study was carried out from 150 °C to 450 °C following the procedure published elsewhere [36]. The external Brønsted acid site concentrations were evaluated by adsorbing 2,6-di-tert-butylpyridine (DTBPy) as a probe molecule (ε_{Bext} = 5.3 cm μmol^{-1}) [37] following the same procedure described above and maintaining an adsorption–desorption equilibrium intervals of 60 min.

Argon physisorption analyses were performed at −186 °C on a Micromeritics 3Flex instrument. The samples were subjected to degasification at 350 °C and under vacuum for 5 h. BET equation was used for the calculation of the surface area, whereas the NL-DFT model was applied to obtain the pore size distribution in the micro- and mesopore ranges and determine the contribution of the different levels of porosity to the textural properties. The total pore volume was calculated at a relative pressure of 0.99.

Solid-state ^{27}Al MAS NMR spectra of the calcined samples were analyzed on a Bruker Advance III/HD 500WB spectrometer using a double-bearing MAS probe (DVT BL4) at a magnetic field of 11.75 T and a resonance frequency of 130.3 MHz. Previous to the analyses, the calcined samples were saturated in water vapor for 16 h. Spectra were recorded at two different spinning rates 10 kHz (2400 scans) and 13.5 kHz (16000 scans) by applying single π/12-pulses (0.6 μs) with a recycle delay of 1 s. The spectra were referenced to the external 1 M aqueous solution of Al(NO$_3$)$_3$. The evaluation of the experimental spectra was carried out with the TopSpin™ 3.2 NMR software package from Bruker BioSpin GmbH.

2.3. Adsorption and catalytic tests

2.3.1. Toluene adsorption–desorption and adsorption-regeneration tests

Toluene adsorption–desorption measurements were carried out using an intelligent gravimetric analyzer (IGA-100, Hiden Isochema ltd.). The IGA instrument consists of a fully computerized microbalance equipped with an ultravacuum system and pressure and temperature controls, which allow accurate measurement of the weight of the samples as a function of the time. The weighing resolution of the balance is 0.1 μg. Previously to the experiments, the sample ($\approx$ 40 mg) was degassed under a vacuum of < 10^{-7} mbar at 400 °C for 3 h. During the experiment, the equilibrium pressures were maintained at the set point by the admittance/exhaust valves controlled by the computer software with an accuracy range of 0.02%. The sample temperature was controlled using the water batch or the heating furnace with an accuracy of 0.1 °C. The adsorption and desorption isotherms were measured at 30 °C, using toluene as a probe molecule, and increasing or decreasing the equilibrium pressure step by step. Approximately 40 points of equilibrium pressures were recorded during the isotherm experiments. The real-time curves of weight uptake changing were also recorded for each equilibrium pressure.

On the other hand, a series of ten adsorption-regeneration cycles followed by a final toluene adsorption–desorption isotherm were performed with one of the dendritic ZSM-5 samples to check its stability. In each cycle, the material was saturated with the adsorbate that was subsequently removed by combining high vacuum (1 h at 30 °C) and thermal (heating at 5 °C min^{-1} up to 400 °C, this temperature being kept constant for 2 h under vacuum) treatments. After the completion of the ten cycles, the toluene adsorption–desorption isotherm was again recorded at 30 °C.

2.3.2. LDPE catalytic cracking

Low-density polyethylene (LDPE) catalytic cracking tests were performed in a stainless-steel stirred batch reactor. In a typical assay, the reactor was loaded with a physical mixture of 10 g of LDPE pellets and 0.1 g of calcined catalyst. The tested catalyst samples were d-ZSM-5 (7d – 150 °C), d-ZSM-5 (10d – 150 °C), h-ZSM-5 and n-ZSM-5. The reactor was closed and heated up to 340 °C under a nitrogen flow (30 mL min^{-1}) at atmospheric pressure. Reaction conditions were maintained for 2 h under stirring. The effluent gaseous stream was passed through an ice condenser to recover the liquid fraction, while the non-condensable gases were collected in a gas sampling bag. Both liquid and gas products were quantified, whereas the amount of residue remaining inside the reactor was weighted for closing the mass-balance.

Liquid and gas products of LDPE catalytic cracking reactions were analyzed in a Varian CP-3800 GC gas chromatograph, employing a 100 m length × 0.25 mm i.d. Chrompack CP SIL PIONA capillary column and FID detector, by the injection of 0.5 mL of the gas fraction and 0.4 μL of the liquid product. Conversions were calculated considering exclusively the product fraction that leaves the reactor with the N$_2$ flow.

2.3.3. Hydrogen production by catalytic methane decomposition

The activity of the zeolitic samples in catalytic methane decomposition (CMD) was evaluated using a simultaneous DSC-TGA thermobalance (TGA-DSC, Mettler-Toledo). As reactive gas, a synthetic CH$_4$ + CO$_2$ mixture with a volume ratio of 60:40 (v:v) was selected in order to mimic biogas composition. The zeolitic sample was loaded into a 150 μL alumina crucible, which was subsequently

introduced into the thermobalance. Reactions were operated under temperature-programmed and isothermal conditions. Before the tests, zeolites were dried at 250 °C with nitrogen. In the case of isothermal reaction tests, the dried samples were heated under 100 mL min^{-1} of nitrogen flow until reaching 965 °C. Then, the reaction was initiated by feeding the synthetic biogas with a flow rate of 50 mL min^{-1}, recording the increase of sample weight along the time due to the deposition of carbon co-produced over the catalysts. In the case of temperature-programmed tests, after drying, the samples were purged under a biogas flow of 50 mL min^{-1}, and the temperature was increased from 50 °C to 1100 °C with a constant heating rate of 10 °C min^{-1}, being kept constant at 1100 °C for 60 min. In these tests, the threshold temperature was determined at the point in which a 0.05% increase in the catalyst weight takes place. Moreover, blank reactions with an empty pan were also carried out, verifying that the contribution of the thermal decomposition of the CH_4 + CO_2 mixture was negligible.

3. Results and discussion

3.1. Synthesis of dendritic ZSM-5

The strategy here applied for the synthesis of dendritic ZSM-5 is based on the emulsion templated aggregative growth of protozeolitic nanounits previously functionalized with an amphiphilic organosilane.

Firstly, the formation of zeolite embryos is induced by precrystallization of the synthesis gel provoking interactions between the zeolite structure directing agent (SDA: tetrapropylammonium cations, TPA$^+$) and the aluminosilicate species. In a recent work [36], we have concluded that these zeolite embryos consist of sub-colloidal particles having simultaneously TPA$^+$ molecules in two configurations: trapped inside and adsorbed over the outer surface of the nano-particles. Thereafter, the amphiphilic organosilane (TPOAC) is added to the synthesis gel. Under specific conditions and compositions, the hydrophobic nature of the C_{18} chain in the TPOAC molecule leads to the formation of an emulsion, in which the interface is stabilized by the already formed embryonic zeolites. Following this synthesis strategy, a number of ZSM-5 samples have been prepared using different crystallization temperatures (150 – 170 °C) and times (1 – 10 days).

TEM images in Fig. 1, taken on samples prepared at different crystallization temperatures and times, reveal that in all cases these materials are formed by oval-shaped particles, with sizes ca. 800 – 1600 nm for the largest dimension and 600 – 900 nm for the smallest one, consisting of aggregates of nanounits with sizes about 10 nm. In contrast with hierarchical ZSM-5 samples prepared with other types of organosilanes or using other synthetic strategies, the nanounits are not randomly assembled but they show a marked radial pattern within the particles. In addition, the occurrence of a high degree of branching, which is a typical feature of dendritic systems, can be clearly observed in the TEM images, where tree-like nanostructures become evident. In the same way, the voids existing between nanorods generate a radially oriented porosity, which is expected to facilitate strongly the access to the internal part of the particles. Another interesting finding is the occurrence of zones within the dendritic aggregates with a low population of nanounits. These cavities or vesicles are clearly appreciated in the inner part of most particles showing sizes in the range 20 – 80 nm. As far as we know, this is the first time that the occurrence of a dendritic nanoarchitecture has been reported for ZSM-5 zeolite.

TPOAC has been earlier used in the literature [38,39] for the preparation of hierarchical ZSM-5 zeolites, but lacking dendritic features. A key step of the synthesis procedure here applied, which

is omitted in previous works, involves the precrystallization of the gel prior to the introduction of the organosilane in order to induce the formation of zeolite embryos. Thus, the characterization of a sample prepared by the addition of TPOAC in the initial synthesis step (Fig. S1) confirms that the dendritic nanoarchitecture is not formed when this precrystallization treatment is not applied. The material so obtained consists of a ZSM-5 sample in which the nanounits are randomly aggregated. Moreover, the XRD pattern of this sample shows the presence of some amorphous material, denoting that the early incorporation of the organosilane affects not only the crystal growth step but also inhibits, at least in part, the formation of the zeolite nuclei.

Furthermore, a series of preliminary experiments were carried out to determine how a number of parameters related to the gel composition affect the appearance of the dendritic morphology (see Fig. S2 and Fig. S3). In this way, one of the key factors is the degree of dilution of the gel. This effect has been confirmed by the preparation of samples varying the water content of the synthesis (H_2O/SiO_2 ratio in the range 25 – 50), while keeping constant the rest of the parameters. As illustrated in Fig. S2, the materials obtained using more diluted gels exhibit fewer dendritic features, which tend to disappear progressively with the increase of the H_2O/SiO_2 molar ratio. In contrast, the results shown in Fig. S3 indicates that the dendritic nanoarchitecture is also observed when increasing the TPA$^+$/SiO$_2$ ratios, i.e. the enhancement of the content of the zeolite SDA is a less critical aspect than that of the water content. However, increasing too much the TPOAC content leads to a less uniform material in terms of particle size and morphology. Finally, adding NaOH to the synthesis gel provokes the formation of a material consisting of both dendritic and non-dendritic particles. These results indicate that the gel composition should be carefully controlled to obtain high-quality dendritic ZSM-5 samples.

3.2. Physico-chemical properties of dendritic ZSM-5

The dendritic ZSM-5 samples are fully crystalline as it can be appreciated in the wide-angle XRD patterns of Fig. 2, displaying the characteristic peaks of the MFI structure with a high intensity and resolution. The crystallinity of these materials is also corroborated by the intense electron diffractions patterns appreciated in the TEM measurements (Fig. 2g). Likewise, high resolution TEM images, taken over the outer part of the aggregates, denote the presence of the diffraction fringes corresponding to the MFI structure (Fig. 2h). The orientation of the diffraction signals is the same through relatively large zones of the dendritic array, which means that the effective size of the crystalline domains is larger than that of the nanounits, explaining the well-defined X-ray pattern of the dendritic ZSM-5 samples. These findings demonstrate that the synthetic strategy here developed leads to the formation of fully crystalline dendritic ZSM-5 materials, even when reducing the crystallization time to 1 day, whereas crystalline/amorphous composites are absent, unlike it occurs during the synthesis of the so-called fibrous zeolites by growing dendritic amorphous silica around zeolite seeds [23,24].

As shown in Fig. S4, d-ZSM-5 samples prepared at different crystallization temperatures exhibit quite similar both TG/DTG profiles and overall weight losses (34 – 40 wt%, referred to the initial sample weight). According to the results obtained in previous works [36,40], the DTG peak at c.a. 460 °C can be assigned to quaternary ammonium species encapsulated within the zeolite micropores, whereas signals at a lower temperature (in the range 200 – 350 °C) would correspond with the thermal decomposition of TPOAC molecules, as well as with the removal of TPA$^+$ species adsorbed on the external surface of the nanounits.

The dendritic nanostructure provides these materials with singular textural properties. This is illustrated in Fig. 3, which displays
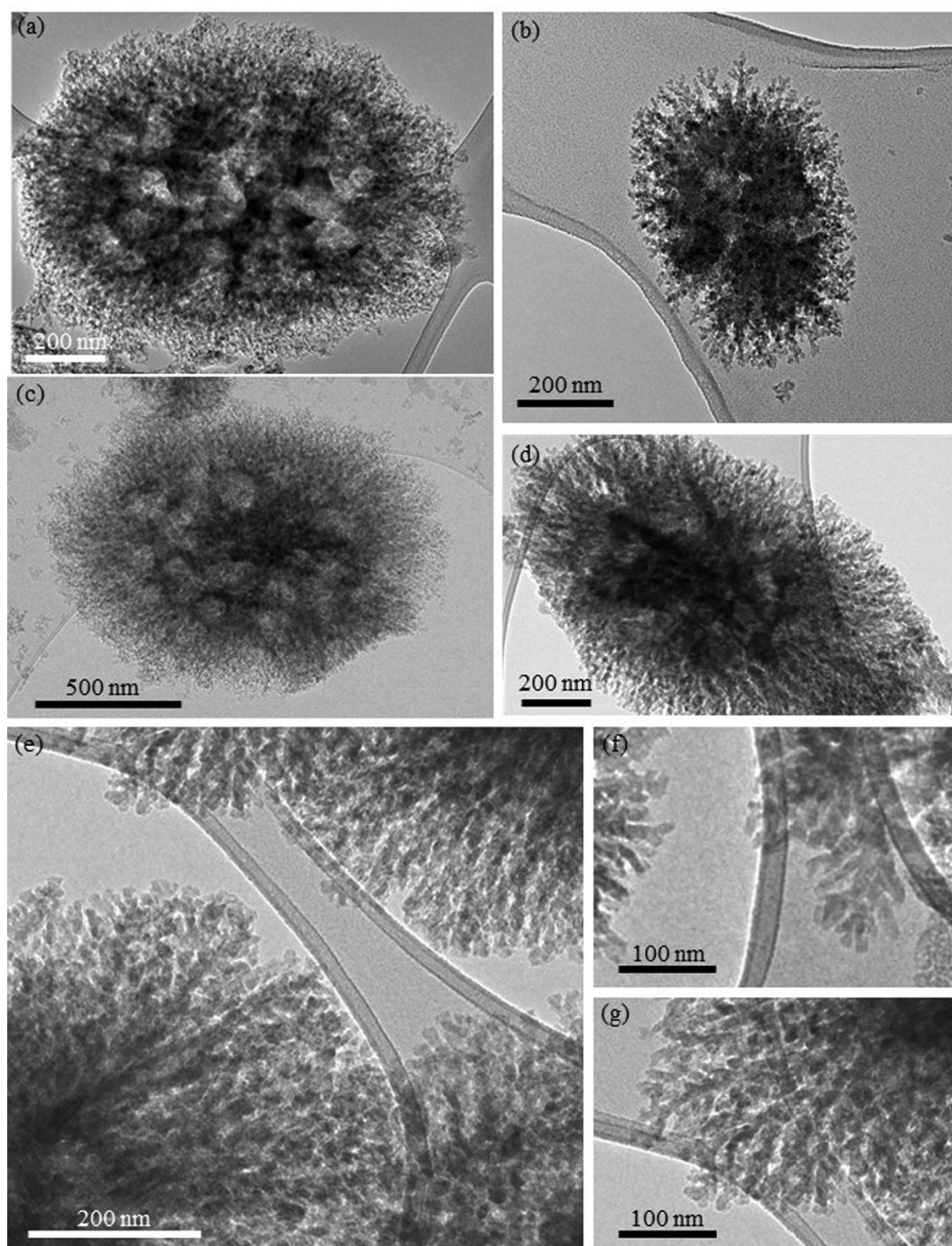
María del Mar Alonso-Doncel, C. Ochoa-Hernández, G. Gómez-Pozuelo et al.

Journal of Energy Chemistry 80 (2023) 77–88

Fig. 1. TEM micrographs of d-ZSM-5 (1d – 150 °C) (a), d-ZSM-5 (1d – 170 °C) (b), d-ZSM-5 (7d – 150 °C) (c), and d-ZSM-5 (7d – 170 °C) (d, e, f, and g) samples.

for different dendritic ZSM-5 samples crystalized at 150 °C the argon adsorption–desorption isotherms at −186 °C, as well as both the pore size distribution (PSD) and the cumulative pore volume obtained applying the NL-DFT method. In the same way, Fig. S5 displays the Ar (-186 °C) adsorption–desorption isotherms, PSD and cumulative pore volume of equivalent samples crystallized at 170 °C. A complex isotherm curve, with three adsorption zones at distinct relative pressure ranges, is observed in all cases showing the presence of different levels of porosity in the same material. This fact is clearly denoted in the PSD, which exhibits a well-defined trimodal porous structure. Thus, in addition to the peak at about 5.5 Å corresponding to the zeolitic micropores, a relatively

narrow mesoporosity (SP1) is present in the range 30 – 100 Å (peak maximum at about 50 – 60 Å). The size of these mesopores is larger than those generated from C_{16} - C_{18} alkyl chain surfactants in MCM-41 materials (about 30 – 35 Å), suggesting the participation of micelle aggregates as templates of the dendritic mesoporosity, similar to what has been earlier reported during the formation of DFNPs [41]. Likewise, the occurrence of larger mesopores (SP2), with a peak maximum of about 200 Å and extending even beyond the meso-macropore limit, is observed in all the dendritic ZSM-5 materials. This last porosity can be associated with the large cavities appreciated within the particles in the TEM images. For both synthesis temperatures, the peak at about 50 – 60 Å in the PSD is
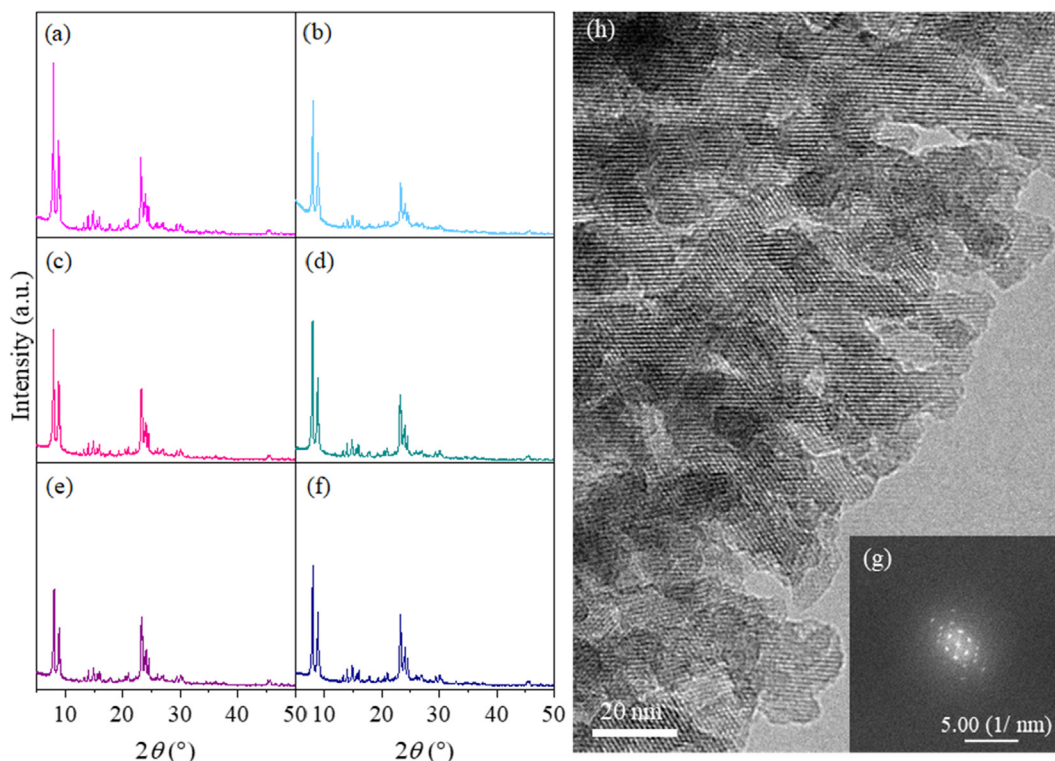
Fig. 2. X-ray diffraction patterns of dendritic calcined d-ZSM-5 (1d – 150 °C) (a), d-ZSM-5 (1d – 170 °C) (b), d-ZSM-5 (7d – 150 °C) (c), d-ZSM-5 (7d – 170 °C) (d), d-ZSM-5 (10d – 150 °C) (e), and d-ZSM-5 (10d – 170 °C) (f) samples, and electron diffraction (g), high-resolution TEM (h) of calcined d-ZSM-5 (7d – 170 °C) sample.

narrower for the samples prepared at a short synthesis time (1 day), denoting that the dendritic nanostructure evolves along the hydrothermal treatment, as commented below when discussing the changes in the textural properties.

In order to get further insights into the different levels of porosity present in dendritic ZSM-5, the samples were also investigated by HAADF-STEM and tilt series acquisition of both TEM and HAADF-STEM micrographs. The images shown in Fig. 4(a and b) and Fig. S6, obtained using dark-field mode and processed according to a rainbow-type color map, evidence a core–shell organization of the dendritic nanostructure. In the central part of the particles, the nanounits show a more random branched arrangement, whereas the radially-oriented nanostructures are preferentially located in the outer zones. More information about the connection and distribution of both zones has been derived by tomographic reconstruction from the tilt series images of a single particle (Fig. 4c and d). Thus, as evidenced by the cross-section image in Fig. 4(d), the large cavities tend to be located mainly on the border between both zones. This result points toward a complex synthesis mechanism, which will be the subject of further studies. Moreover, the high degree of connectivity existing between radially-oriented channels and cavities can be clearly appreciated in the cross-section image, as well as in the tilt series acquisitions (see Supplementary Video file) that provides a 3D visualization of the dendritic nanoarchitecture.

The high connectivity between the multi-level pore system confers these materials with outstanding accessibility. This is expected to facilitate sharply the transport of molecules during their application as catalysts, whereas the trimodal porosity provides voids at different scales for the incorporation of other active phases or components.

As seen in Table 1, the dendritic ZSM-5 samples synthesized during 1, 7, and 10 days exhibit BET surface areas with larger values (between 476 and 630 m^2 g^{-1}) than conventional ZSM-5

(about 400 m^2 g^{-1}), having a large share of mesopore/external surface area. Likewise, important variations can be appreciated in the textural properties associated with the mesoporosity. Thus, the overall mesopore volume varies between 0.390 and 0.809 cm^3 g^{-1}, revealing that it is affected by the crystallization temperature and time. In this way, the d-ZSM-5 (1d – 150 °C) sample shows the highest contribution of the secondary porosity, which also increases the total pore volume, reaching values up to 0.945 cm^3 g^{-1}. For this last material, the average pore volume share corresponding to the multi-level porosity (micropores / mesoporous channels / cavities) is c.a. 15% / 66% / 20%. In overall, a clear trend to decrease the contribution of both types of mesopores along the synthesis time can be appreciated at both temperatures, denoting that the dendritic nanoarchitecture evolves towards more compact configurations during the hydrothermal treatment. Likewise, samples prepared at 150 °C present larger pore volumes for both secondary mesoporosities than those crystallized at a higher temperature. On the other hand, it can be envisaged great possibilities for using dendritic ZSM-5 zeolites as supports of other phases and components, allowing their distribution over the trimodal porosity and facilitating the preparation of hybrid and multifunctional materials.

The generation of the dendritic nanostructure does not negatively affect the Al incorporation, which is an important aspect regarding potential applications as an acid catalyst. In this way, the Si/Al ratio of the dendritic ZSM-5 samples (Table 1) lies in the range 33 – 37, being just slightly higher than that of the gel (31.5), which denotes that both Si and Al are incorporated into the zeolite in a relatively similar extension. ^{27}Al MAS NMR spectra of calcined d-ZSM-5 samples have been used to get insights about the Al coordination (Fig. S7). The major peak at about 54 ppm corresponds with tetrahedral Al, whereas just a minor contribution of octahedral extra-framework species (peak at 0 ppm) is detected. The values of the full width at half maximum (FWHM) of the
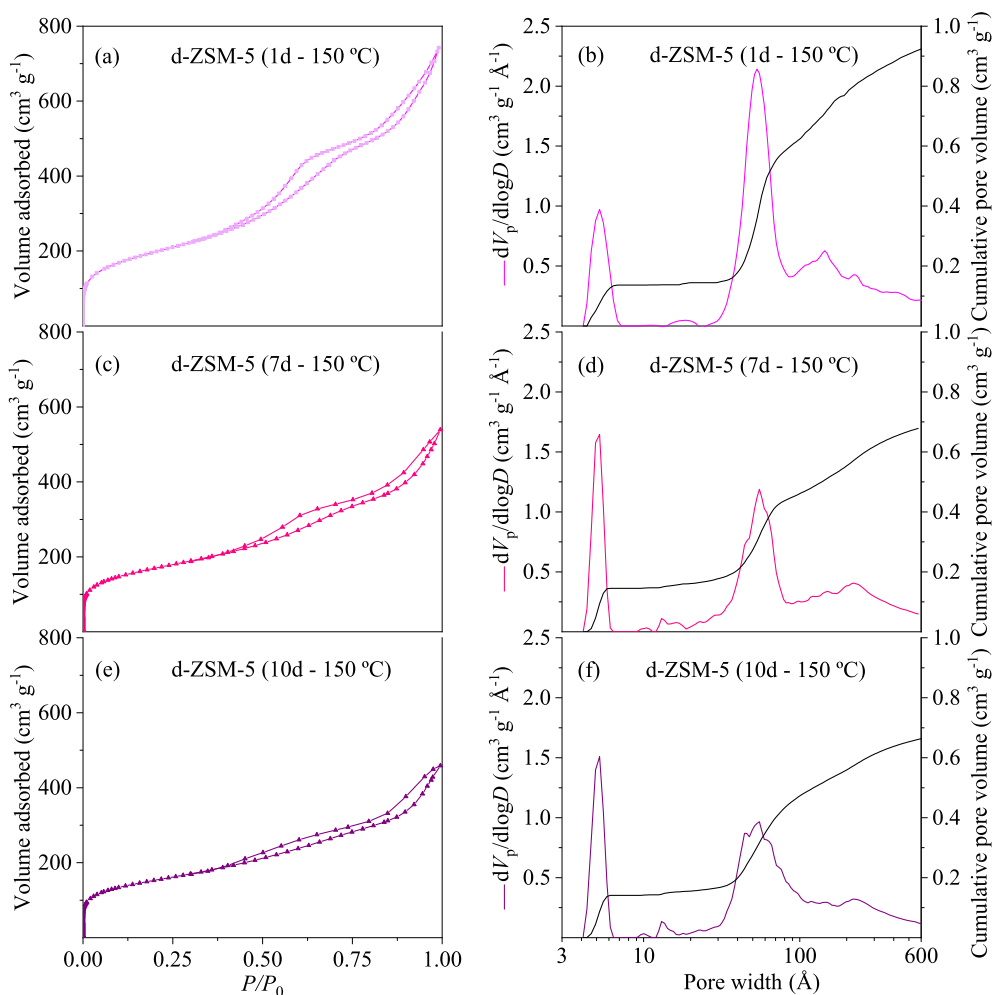
María del Mar Alonso-Doncel, C. Ochoa-Hernández, G. Gómez-Pozuelo et al.

Journal of Energy Chemistry 80 (2023) 77–88

Fig. 3. Argon adsorption–desorption isotherms (a, c and e) and NL-DFT cumulative pore volume and pore size distribution (b, d and f) of dendritic ZSM-5 samples (-186 °C).

tetrahedral peak are about 6.8 – 6.9 ppm, which agrees well with those of highly crystalline ZSM-5 zeolites [42,43]. Therefore, ^{27}Al MAS NMR spectra demonstrate that the features of the Al coordination in the dendritic ZSM-5 materials are very similar to those typically found in high-quality ZSM-5 samples, with a prevalence of tetrahedral framework species.

3.3. Toluene adsorption properties

The potential application of dendritic ZSM-5 materials for the removal of VOCs (volatile organic components) has been assessed by measuring the adsorption–desorption isotherms of toluene vapor at 30 °C (Fig. 5), which is one of the typical components of gasoline. To that end, the behavior of sample d-ZSM-5 (1d – 150 °C), selected due to its high overall pore volume, has been compared with those of two reference MFI materials: nanocrystalline and hierarchical ZSM-5 (n-ZSM-5 and h-ZSM-5, respectively). The main physicochemical properties of the reference samples are provided in Table S1 showing they present a significant (n-ZSM-5) or large (h-ZSM-5) share of external/mesopore surface area, hence they can be considered as materials exhibiting also high accessibility.

As it can be appreciated in Fig. 5(a), the n-ZSM-5 sample exhibits a type I isotherm, according to the IUPAC classification, quickly reaching a plateau at a relative pressure of 0.1 followed by a small increment of adsorption capacity with increasing pressure. On the other hand, the isotherms of d-ZSM-5 (1d – 150 °C) and h-ZSM-5 samples correspond with type IV, showing an initial increase of

adsorption capacity at low relative pressures and the presence of strong hysteresis loops. The maximum adsorption capacity of toluene, measured at a relative pressure of 0.9, was 52% on d-ZSM-5, whereas samples n-ZSM-5 and h-ZSM-5 only adsorbed 13 and 26%, respectively. Furthermore, at an intermediate relative pressure (P/P_0 = 0.6), d-ZSM-5 adsorbed 43% of toluene, while the mass adsorbed by n-ZSM-5 and h-ZSM-5 were just 12 and 23%, respectively. Therefore, the adsorption capacity of toluene on d-ZSM-5 (1d – 150 °C) was much higher than that of the reference materials. This increase in the adsorption capacity can be attributed to the presence of a trimodal porosity and a high total pore volume in the dendritic ZSM-5 samples, as above concluded from the Ar adsorption isotherms. Accordingly, these results denote that dendritic ZSM-5 samples present a high potential for the development of adsorbents in VOCs removal processes.

Since lifetime is an extremely important factor in the use of an adsorbent, adsorption-regeneration cycles followed by toluene adsorption–desorption isotherm were carried out to estimate the lifetime and stability of the d-ZSM-5 sample. Regeneration was accomplished by subjecting the material at a temperature of 400 °C for 2 h under vacuum in each cycle. As shown in Fig. 5(b), after a total of 10 adsorption-regeneration cycles, the toluene adsorption–desorption isotherm was practically the same as that in the first cycle. Thus, just a small decrease in the maximum adsorption capacity (less than 0.5 wt%) was appreciated. These results are indicative of the high stability of d-ZSM-5 along the successive adsorption-regeneration cycles.
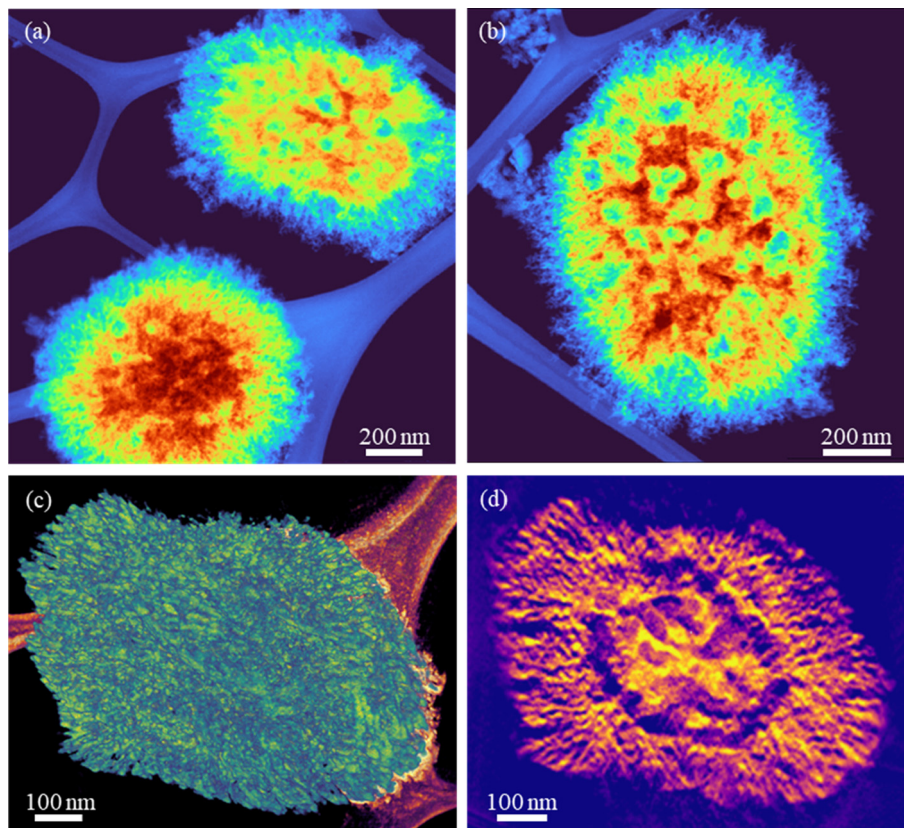
Fig. 4. HAADF-STEM images of d-ZSM-5 (1d – 150 °C), processed according to the rainbow type color map (matter density increase from blue to red) (a and b); tomographic reconstruction volume (c) and cross-section (d).

Table 1
Si/Al ratio and textural properties of dendritic ZSM-5 samples.

Sample	Si/Al	S_{BET}^{a} (m² g⁻¹)	S_{mic}^{b} (m² g⁻¹)	$S_{mes+ext}^{c}$ (m² g⁻¹)	V_T^{d} (cm³ g⁻¹)	V_{mic}^{e} (cm³ g⁻¹)	V_{SP1}^{f} (cm³ g⁻¹)	V_{SP2}^{g} (cm³ g⁻¹)
d-ZSM-5 (1d − 170 °C)	35	495	178	317	0.708	0.11	0.488	0.110
d-ZSM-5 (7d − 170 °C)	37	476	236	240	0.537	0.147	0.233	0.157
d-ZSM-5 (10d − 170 °C)	33	484	227	257	0.584	0.142	0.282	0.160
d-ZSM-5 (1d − 150 °C)	27	630	218	412	0.945	0.136	0.626	0.183
d-ZSM-5 (7d − 150 °C)	36	538	232	306	0.687	0.145	0.315	0.227
d-ZSM-5 (10d − 150 °C)	34	526	226	300	0.663	0.141	0.334	0.188

[a] BET, [b]micropore and [c]mesopore/external surfaces.
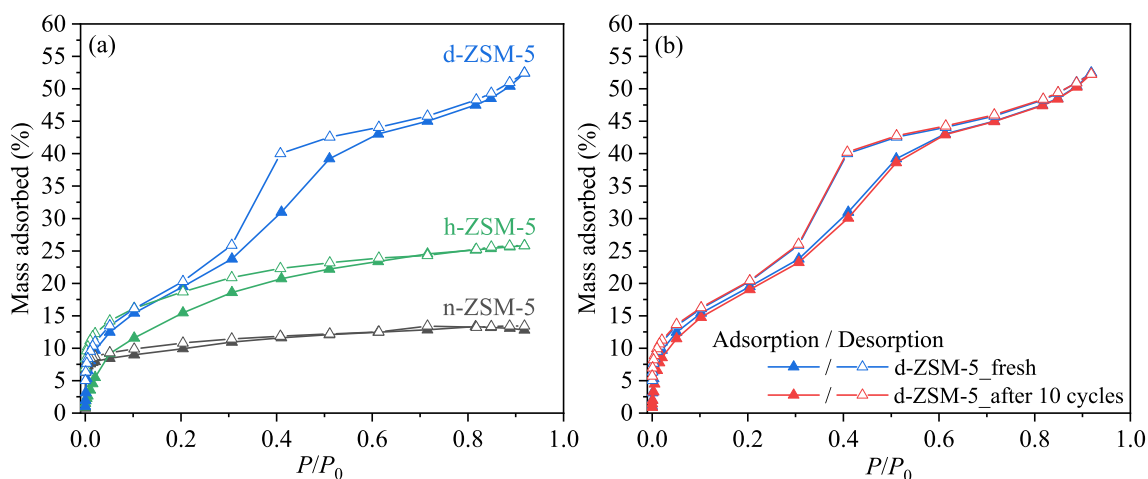[d] Total, [e]micropore and [f,g]secondary mesopore volumes ($V_{SP1} < 100$ Å and $V_{SP2} \geq 100$ Å).

Fig. 5. Adsorption-desorption isotherms of toluene at 30 °C over d-ZSM-5 (1d – 150 °C) and references samples (a). Toluene isotherms over d-ZSM-5 (1d – 150 °C) before and after 10 cycles of adsorption-regeneration treatments (b). (Filled symbols, adsorption; open symbols, desorption).

María del Mar Alonso-Doncel, C. Ochoa-Hernández, G. Gómez-Pozuelo et al.

Journal of Energy Chemistry 80 (2023) 77–88

3.4. Catalytic activity for LDPE cracking

The high accessibility of dendritic ZSM-5 samples makes them very interesting materials as catalysts in reactions suffering from strong steric and diffusional limitations [12,22]. This is the case of the catalytic cracking of polyolefinic plastics due to the bulky nature of the polymeric molecules. Previous literature works have found a good correlation between the catalytic activity of ZSM-5 zeolite and the amount of mesoporous/external surface area [44,45]. In addition, polyolefin cracking is currently a process of high relevance as a route for the valorization of waste plastics. Two of the dendritic ZSM-5 samples prepared in this work (d-ZSM-5 (7d – 150 °C) and d-ZSM-5 (10d – 150 °C)) have been tested in the catalytic pyrolysis of low-density polyethylene (LDPE), being selected based on their high accessibility and suitable acid properties. In addition, the reference samples (h-ZSM-5 and n-ZSM-5) were tested in the same condition. These last materials exhibit a relatively high share of external/mesopore surface (Table S1), which means they present also a high accessibility for the cracking of the LDPE molecules.

Polyolefin cracking reactions are catalyzed by acid sites, with a relevant role being played by Brønsted acidity [46] as it promotes the formation of carbenium ions through the addition of a proton on the polymer macromolecule [47]. The acid sites in conventional ZSM-5 zeolite samples (having crystal sizes in the order of several microns) are mostly Brønsted centres that arise from protons balancing the $[AlO_4]^-$ tetrahedra, their concentration being directly related to the Al content. However, upon calcination, some aluminum atoms are extracted (in part or totally) from the framework forming Lewis acid sites, which may also contribute to the LDPE cracking through the formation of carbenium ions by means of hydride abstraction from the polyolefin [47].

The acidity of both selected and reference ZSM-5 samples has been investigated by pyridine-FTIR (Fig. S8a and b) and DTBPy-FTIR (Fig. S8c) measurements. Dendritic ZSM-5 samples exhibit a lower concentration of Brønsted acid sites (BAS) in comparison with the reference materials. At least in part, this fact could be assigned to variations in the Si/Al ratio (34–36 in the dendritic samples versus 30 in the reference zeolites). However, both d-ZSM-5 zeolites possess a content of Lewis acid sites (LAS) higher than that of the reference samples. Therefore, these significant differences in the content and distribution of acid sites can be related also to the larger share of external/mesopore surface area of the dendritic samples in comparison with n/h-ZSM-5 materials. This

finding is in agreement with previous literature reporting a reduction of the Brønsted/Lewis ratio in ZSM-5 zeolite as the external/mesopore surface is increased since the latter favors the conversion of BAS into LAS during the calcination treatment [48]. In any case, it is interesting to note that the d-ZSM-5 samples exhibit a strong acidity as indicated by the presence of pyridine adsorbed on both Brønsted and Lewis acid sites after evacuation at 350 °C.

The results shown in Fig. 6(a) clearly denote the effectiveness of the dendritic nanoarchitecture in the catalytic cracking of large molecules like LDPE. The dendritic ZSM-5 samples lead to quite higher plastic cracking activities than both reference materials when using either the Brønsted acid sites or the overall acid sites concentration as reference. Thus, the LDPE converted per unit of BAS + LAS concentration is about three fold higher for the dendritic zeolite samples than in the case of the nano-crystalline ZSM-5. This result can be assigned to the larger mesopore/external surface of the former. In the same way, the better performance of the dendritic ZSM-5 samples regarding the hierarchical one can be related at least in part to their higher mesopore/external surface area (248 m^2/ g^{-1} for h-ZSM-5 sample versus 300 – 306 m^2 g^{-1} for dendritic samples). However, this variation is not enough to account for the observed strong enhancement of the catalytic activity exhibited by the dendritic ZSM-5 samples in comparison with the hierarchical one. In this way, the determination of the relative concentration of external Brønsted acid sites by DTBPy-FTIR indicated that the dendritic samples showed a quite more accessible acidity than both reference zeolites as can be appreciated in Fig. S8(c). This fact, together with the large size and high connectivity of the mesopores in the dendritic samples, are the main factors responsible for their outstanding activity in this reaction.

Light olefins are the main products of the LDPE catalytic cracking for both dendritic and reference ZSM-5 materials. They are primary products obtained by end-chain cracking reactions, which are promoted by the strong ZSM-5 acidity. Once formed, light olefins can undergo a variety of transformations leading to larger olefins, paraffins, isoparaffins, naphthenes and aromatics. Accordingly, the product distribution by carbon atom number obtained in the LDPE catalytic cracking (Fig. S9) denotes two main contributions: i) light hydrocarbons (C$_2$-C$_5$, mainly olefins) formed by cracking reactions at the end of the polymeric chains, and ii) gasoline range hydrocarbons (C$_6$ – C$_{10}$) produced from the primary cracking products, mainly through oligomerization, cyclization, aromatization and isomerization reactions.

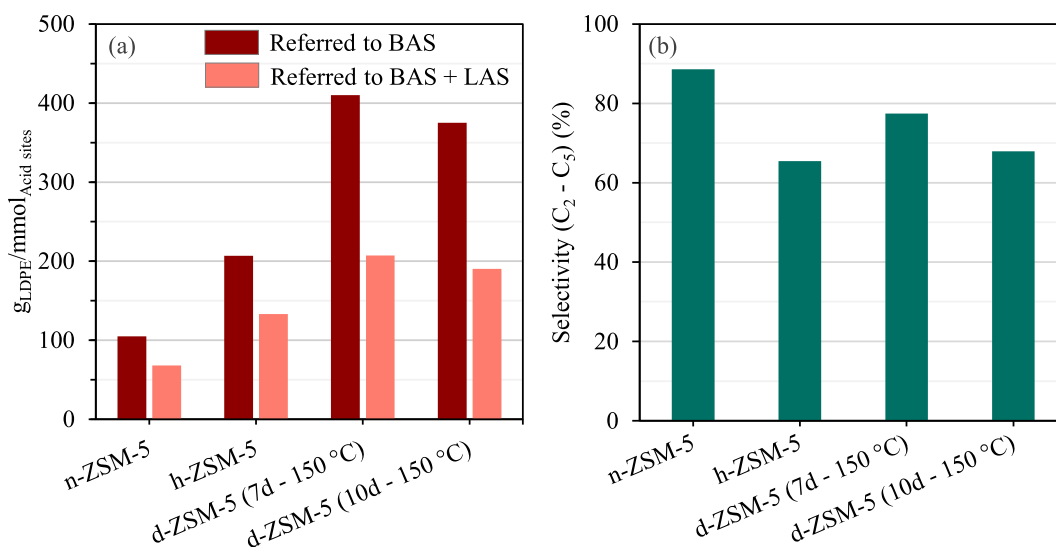**Fig. 6.** LDPE catalytic cracking over dendritic, hierarchical and nanocrystalline ZSM-5 samples (T = 340 °C; P/C (w/w) = 100). LDPE mass converted referred to the amount of Brønsted and total acid sites (a). Selectivity to primary cracking products (C$_2$-C$_5$ hydrocarbons) (b).

Unexpectedly, the dendritic ZSM-5 samples exhibit a selectivity pattern more similar to that of the nanocrystalline sample than the one observed for the hierarchical zeolite. Likewise, it can be appreciated in Fig. 6(b) that the overall selectivity towards end-chain cracking products (C$_2$-C$_5$ hydrocarbons) varies according to the following trend: n-ZSM-5 (90%), d-ZSM-5 (66–75%) and h-ZSM-5 (63%). The comparison between the two reference samples follows the expected variation, i.e. the material with higher catalytic activity (h-ZSM-5 > n-ZSM-5) exhibits also a lower selectivity towards primary cracking products (h-ZSM-5 < n-ZSM-5) as it has been earlier observed in the literature [40]. However, this is not the case when assessing the results obtained with the dendritic ZSM-5 samples. Considering the quite superior activity of the latter in comparison with the hierarchical ZSM-5 sample, one would expect that the extension of secondary reactions is significantly favored over d-ZSM-5 materials. On the contrary, the results in Fig. 6(b) denote that the dendritic samples are more selective for the production of C$_2$ – C$_5$ hydrocarbons than the hierarchical zeolite. This apparently anomalous result can be considered as a consequence of the singular multi-level porosity of the dendritic ZSM-5 samples, with large mesopore dimensions and a high degree of connectivity, which favors the outwards transport of the light olefins and paraffins formed in the primary cracking reactions, thus attenuating its subsequent conversion. As a result, the dendritic ZSM-5 materials allow the LDPE cracking reactions to proceed with a sharp enhancement in the selectivity towards primary products.

3.5. Catalytic activity for hydrogen production through methane decomposition

Methane decomposition (CH$_4$ (g) → C(s) + 2H$_2$ (g)) is a reaction with high interest for the production of clean hydrogen, i.e. free of CO$_2$ emissions since the carbon so formed is stored in solid form. Moreover, when applied to bio-methane or biogas, the overall carbon balance can be negative, having a CO$_2$ fixation effect. Accordingly, biogas decomposition is one of the few processes that may induce a negative carbon balance.

The use of catalysts for methane decomposition (catalytic methane decomposition, CMD) boosts the reaction rate affording to work at temperatures significantly below that required in the thermal methane decomposition (over 1300 °C). Methane decomposition involves the co-production of a great amount of carbon, representing 75 wt% of the methane being reacted according to the stoichiometry, which is deposited over the catalyst. Unlike it occurs with coke formation during the transformation of organic compounds, the generation of carbon during CMD cannot be avoided since it is one of the two main products obtained in the reaction. Therefore, one of the major challenges in CMD is the development of catalysts with a strong resistance to deactivation. In this way, the CMD process can be also employed as an accelerated deactivation test to determine the ability of the catalysts to withstand the deposition of high amounts of carbon. In a previous work [49], the catalytic activity of different pure silica materials, including two samples of silicalite-1 (pure silica MFI zeolite), have been assessed for CMD, showing it is largely determined by their porous properties. This result has prompted us to investigate the performance in CMD of dendritic d-ZSM-5 (1d – 150 °C), selected due to its large total pore volume as it may facilitate the formation and growth of carbon deposits, being compared with those of the reference n-ZSM-5 and h-ZSM-5 materials.

The three materials were first assayed in the CMD reaction under temperature-programmed conditions (Fig. 7a), which allowed the determination of the threshold temperature (T_{th}), i.e. the minimum temperature for the reaction to proceed. The tests were performed in a thermobalance feeding a CH$_4$ + CO$_2$ mixture, which allows the reaction progress to be continuously monitored through the increase of the catalyst weight provoked by the carbon deposition on the catalyst surface (W_{Cdep}). Both d-ZSM-5 and
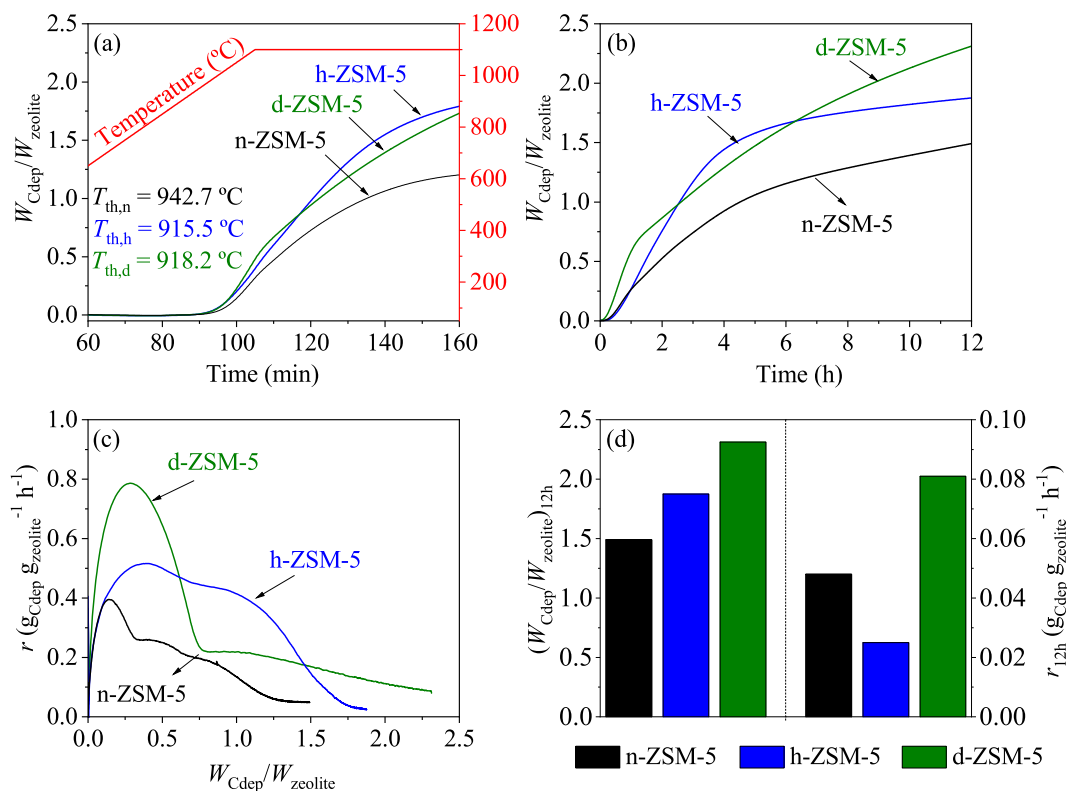

Fig. 7. Methane catalytic decomposition tests over d-ZSM-5 (1d-150 °C), n-ZSM-5 and h-ZSM-5 samples: carbon formation in temperature programmed experiments (a), carbon formation in isothermal (T = 965 °C) experiments (b), reaction rate (r) versus carbon deposition ratio ($W_{Cdep}/W_{zeolite}$) in isothermal tests (c), overall carbon deposition and reaction rates at 12 h for the isothermal tests (d).

María del Mar Alonso-Doncel, C. Ochoa-Hernández, G. Gómez-Pozuelo et al.

Journal of Energy Chemistry 80 (2023) 77–88

h-ZSM-5 materials present close T_{th} values ($T_{th,h}$ = 915.5 °C and $T_{th,d}$ = 918.2 °C for h-ZSM-5 and d-ZSM-5 (1d – 150 °C), respectively), which are significantly lower than that of the n-ZSM-5 (942.7 °C), showing that this parameter is determined mainly by the mesopore/external surface area. This can be connected with the occurrence on the mesopore/external surface of a great concentration of terminal silanol groups, which have been identified in previous work as precursors of the actual active sites (Si-C moieties) [49].

On the other hand, important differences were appreciated in the performance of the three catalysts under isothermal conditions (T = 965 °C). In these tests (Fig. 7b), the dendritic ZSM-5 exhibits clearly a superior activity in comparison with the reference materials, leading to higher carbon deposition ratios at both short and long reaction times. The marked change in the slope of the curve, present in Fig. 7(b) for the d-ZSM-5 (1d – 150 °C) sample at about 1 h of time on stream, can be related to its narrow SP1 mesopore size distribution (see Fig. 3) since it has been earlier also observed in CMD for materials having uniform mesopores (SBA-15 and CMKs carbons) [49,50].

The profile of the curves in Fig. 7(c), representing the reaction rate versus the carbon deposition ratio, provides additional information about the ability of the samples to withstand the carbon deposition. The increasing initial reaction rate is probably originated by the progressive formation of the Si-C sites, although some autocatalytic effects induced by the own carbon deposits cannot be neglected, in agreement with previous literature [51]. At longer reaction times, the reaction rate starts decreasing due to the accumulation of the carbon deposits over the surface and porosity of the catalysts. In this way, in the case of the d-ZSM-5 sample the two signals observed in this curve would correspond with the filling of the two types of mesoporosities present in this sample: radially oriented mesopores and cavities. Two contributions can be also observed in this figure for the h-ZSM-5 sample, although in this case highly overlapped, which can be assigned to the relatively broad pore size distribution present for this material in the mesopore range (Fig. S10).

Interestingly, at long times on stream (12 h), the dendritic ZSM-5 sample still retains a significant activity in spite of having been subjected to a higher carbon deposition ratio than the reference materials. This can be also seen in Fig. 7(d) which compares the values of the reaction rate and the carbon deposition ratio for the three materials after 12 h of time on stream.

The methane decomposition activity depends not only on the mesopore volume available for the formation of the carbon deposits but also on the mesopore size. Since n-ZSM-5 is formed by nanocrystals with sizes in the range 40 – 80 nm, the intercrystalline spaces are quite larger than the mesopores present in the h-ZSM-5 sample. Accordingly, the latter becomes blocked in a higher extension as the carbon deposits are accumulated at long reaction times in comparison with the nanocrystalline sample. The quite superior performance of the d-ZSM-5 (1d – 150 °C) sample can be linked to its large pore volume and high connectivity between the different types of mesoporosity, which facilitate the growth of the carbon deposits towards the outer part of the zeolite particles, thus attenuating their deactivation effects. This result shows the high potential of dendritic ZSM-5 materials for the development of catalysts in processes suffering from strong carbon/coke deposition phenomena.

4. Conclusions

ZSM-5 zeolite with a dendritic 3D nanoarchitecture has been synthesized by hydrothermal crystallization of zeolite embryos previously functionalized with an amphiphilic organosilane. Dendritic ZSM-5 is formed by a radial-oriented assembly of small nanounits (10 nm) that extends, with significant branching, across the zeolite particles. Although the mechanism of the crystallization of dendritic ZSM-5 zeolite will be studied in future works, it can be envisaged that it follows a quite complex process in which the formation of a fine emulsion plays a fundamental role in directing the branched and radial aggregative growth of the zeolite nanounits into a dendritic nanoarchitecture.

The dendritic ZSM-5 samples exhibit singular properties, showing a well-defined and highly interconnected trimodal porosity: zeolitic micropores, mesoporous channels and meso-macroporous cavities. The highest total pore volume (0.945 cm³ g⁻¹) corresponds with the material obtained at 150 °C and 1 day of crystallization. As a consequence, dendritic ZSM-5 possesses a quite enhanced adsorption of toluene vapor in comparison with reference ZSM-5 samples, showing its high potential for VOCs removal applications.

Investigation of the samples by HAADF-STEM, tilt series acquisition and tomographic reconstruction evidence the high degree of connectivity existing between cavities and radially-oriented channels. This fact imparts these materials with a remarkable accessibility to facilitate the transport of molecules during their application as catalysts.

The dendritic nanostructure provides ZSM-5 zeolite with outstanding catalytic activity for LDPE cracking, while maintaining a high selectivity towards primary products (C_2-C_5 hydrocarbons) since their outwards transport is favored by the large size and high connectivity of the multi-level porosity. These products correspond mostly with light olefins that could be used as raw chemicals, thus promoting the chemical recycling of polyolefinic plastic wastes, in addition to the production of fuels.

Likewise, dendritic ZSM-5 has shown a good performance in the generation of hydrogen by methane catalytic decomposition, retaining a significant activity at long reaction times even after being subjected to strong carbon deposition. These results can be attributed to the large pore volume and high connectivity between the different types of mesoporosity in this material, which facilitate the growth of the carbon deposits towards the outer part of the zeolite particles, thus attenuating their deactivation effects.

Declaration of competing interest

The authors declare that they have no known competing financial interests or personal relationships that could have appeared to influence the work reported in this paper.

Acknowledgments

Appendix A. Supplementary material

Supplementary data to this article can be found online at https://doi.org/10.1016/j.jechem.2023.01.023.

References

[1] A. Maity, V. Polshettiwar, ChemSusChem 10 (2017) 3866–3913.
[2] P. Hao, B. Peng, B.Q. Shan, T.Q. Yang, K. Zhang, Nanoscale Adv. 2 (2020) 1792–1810.
[3] Y. Wang, X. Du, Z. Liu, S. Shi, H. Lv, J. Mater. Chem. A 7 (2019) 5111–5152.
[4] Y. Wang, J. Zhou, B. Zhang, L. Tian, Z. Ali, Q. Zhang, Chem. Eng. J. 327 (2017) 932–940.
[5] Y.R. Lee, S. Zhang, K. Yu, J. Choi, W.S. Ahn, Chem. Eng. J. 378 (2019).
[6] L.Y. Yuan, G. Gao, C.Q. Feng, Z.F. Chai, W.Q. Shi, Chem. Eng. J. 385 (2020).
[7] A. Primo, H. Garcia, Chem. Soc. Rev. 43 (2014) 7548–7561.
[8] M.E. Davis, Chem. Lett. 26 (2014) 239–245.
[9] J. Shi, Y. Wang, W. Yang, Y. Tang, Z. Xie, Chem. Soc. Rev. 44 (2015) 8877–8903.
[10] J. Jiang, J. Yu, A. Corma, Angew. Chem. Int. Ed. 49 (2010) 3120–3145.
[11] H. Dai, Y. Shen, T. Yang, C. Lee, D. Fu, A. Agarwal, T.T. Le, M. Tsapatsis, J.C. Palmer, B.M. Weckhuysen, P.J. Dauenhauer, X. Zou, J.D. Rimer, Nat. Mater. 19 (2020) 1074–1080.
[12] P. Peng, X.H. Gao, Z.F. Yan, S. Mintova, Natl. Sci. Rev. 7 (2020) 1726–1742.
[13] R. Jain, A. Chawla, N. Linares, J. García Martínez, J.D. Rimer, Adv. Mater. 33 (2021) 1–8.
[14] J. Pérez-Ramírez, C.H. Christensen, K. Egeblad, C.H. Christensen, J.C. Groen, Chem. Soc. Rev. 37 (2008) 2530–2542.
[15] D.P. Serrano, J.M. Escola, P. Pizarro, Chem. Soc. Rev. 42 (2013) 4004–4035.
[16] S. Mintova, M. Jaber, V. Valtchev, Chem. Soc. Rev. 44 (2015) 7207–7233.
[17] M. Hartmann, M. Thommes, W. Schwieger, Adv. Mater. Interfaces 8 (2021) 2001841.
[18] U. Díaz, A. Corma, Dalt. Trans. 43 (2014) 10292–10316.
[19] W.J. Roth, P. Nachtigall, R.E. Morris, J. Čejka, Chem. Rev. 114 (2014) 4807–4837.
[20] M. Shete, M. Kumar, D. Kim, N. Rangnekar, D. Xu, B. Topuz, K.V. Agrawal, E. Karapetrova, B. Stottrup, S. Al-Thabaiti, S. Basahel, K. Narasimharao, J.D. Rimer, M. Tsapatsis, Angew. Chem. Int. Ed. 56 (2017) 535–539.
[21] J. Přech, P. Pizarro, D.P. Serrano, J. Čejka, Chem. Soc. Rev. 47 (2018) 8263–8306.
[22] M. Hartmann, A.G. Machoke, W. Schwieger, Chem. Soc. Rev. 45 (2016) 3313–3330.
[23] L.P. Teh, S. Triwahyono, A.A. Jalil, M.L. Firmansyah, C.R. Mamat, Z.A. Majid, Appl. Catal. A Gen. 523 (2016) 200–208.
[24] M.L. Firmansyah, A.A. Jalil, S. Triwahyono, H. Hamdan, M.M. Salleh, W.F.W. Ahmad, G.T.M. Kadja, Catal, Sci. Technol. 6 (2016) 5178–5182.
[25] H.U. Hambali, A.A. Jalil, S. Triwahyono, S.F. Jamian, N.A.A. Fatah, A.A. Abdulrasheed, T.J. Siang, Int. J. Hydrogen Energy 46 (2021) 24652–24665.
[26] L. Wang, S.C. Zhu, M.K. Shen, H.W. Tian, S.H. Xie, H. Bin Zhang, Y.H. Zhang, Y. Tang, Angew. Chem. Int. Ed. 56 (2017) 11764–11768.
[27] M.S. Kumar, M. Schwidder, W. Grünert, A. Brückner, J. Catal. 227 (2004) 384–397.
[28] N. Rahimi, R. Karimzadeh, Appl. Catal. A Gen. 398 (2011) 1–17.
[29] Y.-T. Cheng, G.W. Huber, Green Chem. 14 (2012) 3114–3125.
[30] D.P. Serrano, J. Aguado, J.M. Escola, J.M. Rodríguez, A. Peral, Chem. Mater. 18 (2006) 2462–2464.
[31] J.M. Escola, D.P. Serrano, J. Aguado, A. Peral, J.M. Rodriguez, J. Mater. Chem. 18 (2008) 4210–4218.
[32] J. Ahrens, B. Geveci, C. Law, ParaView : An End-User Tool for Large-Data Visualization, 2005.
[33] B.D.A. Levin, Y. Jiang, E. Padgett, S. Waldon, C. Quammen, C. Harris, U. Ayachit, M. Hanwell, P. Ercius, D.A. Muller, R. Hovden, Micros. Today 26 (2018) 12–17.
[34] M.D. Hanwell, U. Ayachit, D.A. Muller, htpps://tomviz.org. (Last date access July 14th, 2022).
[35] C.A. Emeis, J. Catal. 141 (1993) 347–354.
[36] M. Alonso-Doncel, A. Peral, C. Ochoa-Hernández, R. Sanz, D. Serrano, J. Mater. Chem. A 9 (2021) 13570–13587.
[37] M. Shamzhy, B. Gil, M. Opanasenko, W.J. Roth, J. Čejka, ACS Catal. 11 (2021) 2366–2396.
[38] M. Li, I.N. Oduro, Y. Zhou, Y. Huang, Y. Fang, Micropor. Mesopor. Mater. 221 (2016) 108–116.
[39] Y. Zhang, S. Che, Angew. Chem. Int. Ed. 59 (2020) 50–60.
[40] M. Alonso-Doncel, A. Peral, M. Shamzhy, J. Čejka, R. Sanz, D.P. Serrano, Micropor. Mesopor. Mater. 303 (2020).
[41] P.C. Liu, Y.J. Yu, B. Peng, S.Y. Ma, T.Y. Ning, B.Q. Shan, T.Q. Yang, Q.S. Xue, K. Zhang, P. Wu, Green Chem. 19 (2017) 5575–5581.
[42] E. Oldfield, J. Haase, K.D. Schmitt, S.E. Schramm, Zeolites 14 (1994) 101–109.
[43] M. Alonso-Doncel, A. Peral, M. Shamzhy, J. Čejka, R. Sanz, D.P. Serrano, Catal. Today 345 (2020) 27–38.
[44] D.P. Serrano, J. Aguado, J.M. Escola, ACS Catal. 2 (2012) 1924–1941.
[45] I. Vollmer, M.J.F. Jenks, R. Mayorga González, F. Meirer, B.M. Weckhuysen, Angew. Chem. Int. Ed. 60 (2021) 16101–16108.
[46] A. Peral, J.M. Escola, D.P. Serrano, J. Přech, C. Ochoa-Hernández, J. Čejka, Catal. Sci. Technol. 6 (2016) 2754–2765.
[47] L. Yao, J. Zhu, S. Li, Y. Ma, C. Yue, J. Therm. Anal. Calorim. 147 (2022) 14257–14266.
[48] D.P. Serrano, G. Vicente, M. Linares, J. Catal. 279 (2011) 366–380.
[49] D.P. Serrano, J.A. Botas, P. Pizarro, I. Moreno, G. Gómez, Int. J. Hydrogen Energy 40 (2015) 5237–5243.
[50] J.A. Botas, D.P. Serrano, R. Guil-López, P. Pizarro, G. Gómez, Int. J. Hydrogen Energy 35 (2010) 9788–9794.
[51] D.P. Serrano, J.Á. Botas, P. Pizarro, G. Gómez, Int. J. Hydrogen Energy 38 (2013) 5671–5683.